A Numerical Investigation of Wind Tunnel Model Deformations Caused by the Twin-Sting Support System

R. Flores, E. Ortega, E. Oñate

A Numerical Investigation of Wind Tunnel Model Deformations Caused by the Twin-Sting Support System

R. Flores
E. Ortega
E. Oñate

A NUMERICAL INVESTIGATION OF WIND TUNNEL MODEL DEFORMATIONS CAUSED BY THE TWIN-STING SUPPORT SYSTEM.

Roberto Flores, Enrique Ortega and Eugenio Oñate

International Center for Numerical Methods in Engineering (CIMNE)
Universidad Politécnica de Cataluña
Edificio C1, Campus Norte, UPC
Gran Capitán, s/n, 08034 Barcelona, España

Abstract. This work presents a wing deformation analysis of a twin-sting-mounted commercial aircraft model. Twin-sting arrangements minimize flow disturbances around the model fuselage and tail; on the other hand, they cause important changes in the flow field around the wing and also increase aerodynamic interference at the wing and aeroelastic effects on the wing. In some cases, these effects can alter the normal downwash developed behind the wing, modifying the flow pattern at the tail. Consequently, when tail aerodynamics is a major concern, this kind of support interference should be carefully evaluated. The methodology developed in this work employs an unstructured FEM-based flow solver for computing aerodynamic loads. These loads are then transferred to a finite element structural model in order to assess the geometrical deformation of the wing caused by the torsional moment exerted by the supporting mechanism. The analysis described involves three different twin-sting support configurations taking into account angle of attack variations and Mach numbers spanning from subsonic to high transonic ranges.

1. INTRODUCTION

Nowadays the global aircraft industry is faced with important challenges. New commercial aircraft developments should be aimed at combining lower manufacturing and overhead costs as well as reduced environmental impact (mainly fuel consumption, noise and gas emissions) with improved flight and cargo capabilities. This scenario demands the aircraft industry important advances in technology and design. As a first step to achieve these goals, the development and application of enhanced prediction and analysis techniques during early aircraft design stages has played a major role over the last decades. Along the same lines, the Rear-Fuselage and Empennage Flow Investigation (REMFI) project [1] was conceived. This project was carried out by investigation groups from the industrial, research and academic fields coordinated by Airbus Spain within the European Commission (EC) 6th Framework Programme. Before presenting our work, we will briefly describe the main characteristics of the REMFI project.

The REMFI project was mainly aimed at studying, modelling and simulating tail and rear fuselage aerodynamics for a large commercial jet, pointing at providing the European aircraft industry with mechanisms to exploit advances coming from applied research at early design stages. In addition, the REMFI project was also intended to satisfy an increasing demand for further investigation on tail flow phenomena. The fact that innovative empennage design is one of the areas in which important advances are expected is what mainly motivates the growing actual interest in this field.

The complex nature of the flow field and the huge scale of the computational models involved in the project demanded the REMFI partners considerable efforts in developing numerical and experimental analysis tools. Although CFD and structural analysis codes are now widely-accepted tools for design, important difficulties arise when extremely large computational models involving complex flow behaviour must be undertaken. The numerical issues that had to be faced in this project were mainly related to geometry and mesh generation, CPU-runtime and memory requirements and reliable characterization of complex flow phenomena (e.g. turbulence modelling and negative tail stall involving massive boundary layer separation).

In addition, the development of the project also required extensive experimental validation. To this effect two wind tunnel test campaigns were planned. The first one, targeting low Reynolds number regimes was carried out in the Aircraft Research Association wind tunnel (ARA). A second campaign, projected to measure aerodynamic characteristics under flight conditions, was conducted in the European Transonic Wind Tunnel (ETW). It should be noticed that the same test model, only with minor modifications, was employed in both campaigns.

The planning and execution of the wind tunnel tests brought about important challenges. The testing envelope covered a wide range of tail settings, Mach and Reynolds numbers and a high accuracy was required for measuring the force acting on the tail. To achieve the sought accuracy a non-standard *live-rear-end* measuring technique was adopted. This technique uses a mechanically separate rear end section attached to the main body through internal balances allowing direct measurement of the force acting on the tail. This mechanical setup precludes the use of a conventional tail cone-attached sting. A wing-attached twin-sting mounting was chosen bringing the added benefit of aerodynamic interference effects on the empennage.

The present work, which is part of a broader investigation developed during the REMFI project, focuses on the study of wing model deformation due to the twin-sting support

mechanism with an emphasis on wing torsion and bending. There has always been some level of uncertainty associated with the possibility of increased aeroelastic coupling due to wing deformation when using the twin-sting arrangement. The resulting change in spanwise lift distribution could possibly lead to degraded overall accuracy in tail flow field measurements. Surprisingly, the issue has not been previously investigated in depth. As part of the REMFI effort to improve the understanding of tail flow it was necessary to asses magnitude of wing *deformation when using twin stings. Of special interest was the change in wing twist when* using the twin-stings. under test conditions. There was a widespread concern with the possibility of increased torsional deformations which, through the change in downwash, could disrupt the flow field at the tail negating the benefits of the twin-sting rig. In fact, not only the accuracy of tail force measurements is at stake, but also the structural integrity of the test model. This paper focuses on the change in magnitude of wing twist when moving from the standard configuration (fuselage-attached sting) to the twin-sting setup.

The work is organized as follows. The flow solver employed for calculating the aerodynamic loads causing wing model deformation is described in Section 2 and the computational setup to be analyzed is presented in Section 3. Next, the structural modelling and the fluid-structure coupling procedure are explained in Section 4 and the wing deformation assessment is developed in Section 5. Finally, the most relevant conclusions of this work are presented in Section 6.

2. THE FLOW SOLVER

To calculate the flow field around the test model a Euler solver has been developed. Because deformations caused by the viscous stresses are of small importance, the pressure field obtained from the inviscid solution is sufficient to yield accurate model deformations. The geometries to be analyzed are complex so the computational models contain a large number of degrees of freedom. Thus, solver efficiency and ease of grid generation become topics of major importance. In this work, an edge-based scheme for solving the compressible flow equations on unstructured finite element grids is employed. This solver, developed at CIMNE [2] has been optimized for running in shared memory parallel architectures using OPEN-MP directives minimizing memory access overheads and cache misses. In this section the numerical scheme adopted for solving the three-dimensional compressible flow equations is presented.

2.1 The Euler equations

The three-dimensional set of Navier-Stokes equations can be written in conservative form (neglecting body force terms) as follows

$$\frac{\partial \mathbf{U}}{\partial t} + \frac{\partial \mathbf{F}_k}{\partial x_k} + \frac{\partial \mathbf{G}_k}{\partial x_k} = 0 \quad k=1,3 \tag{1}$$

where $\mathbf{U}$ is the conservative variables vector and $\mathbf{F}_k$ and $\mathbf{G}_k$ are the advective and diffusive flux vectors in the spatial direction x_k respectively. These vectors are defined as

$$\mathbf{U} = \begin{bmatrix} \rho \\ \rho u_i \\ \rho e_t \end{bmatrix} \quad , \quad \mathbf{F}_k = \begin{bmatrix} \rho u_k \\ \rho u_i u_k + \delta_{ik} p \\ (\rho e_t + p) u_k \end{bmatrix} \quad , \quad \mathbf{G}_k = \begin{bmatrix} 0 \\ -\tau_{ik} \\ q_k - \tau_{kj} u_j \end{bmatrix} \tag{2}$$

where ρ, p and e_t respectively denote the density, pressure and total energy of the fluid; u_i is the i-component of the velocity vector, δ_{ij} is the Kronecker delta and indices i,j,k range from 1 to 3. By setting $\mathbf{G}_k=0$ the Euler equations are obtained. Assuming ideal gas behaviour the equation of state which serves as closure is

$$p = \rho(\gamma - 1)\left[e_t - \frac{1}{2} u_i u_i \right] \tag{3}$$

with $\gamma = c_p/c_v$ being the ratio of specific heats (in the present work we adopt $\gamma=1,4$). Additionally, in order to solve the system of equations (1) over a closed domain Ω with closed boundary Γ for a given time t proper initial and boundary conditions must be defined.

2.2 Finite Element discretization

The weak form of the Euler equations (1) can be expressed as

$$\int_\Omega \mathbf{W}(x)\left(\frac{\partial \mathbf{U}}{\partial t} + \frac{\partial \mathbf{F}_k}{\partial x_k} \right) d\Omega = 0 \quad \forall \mathbf{W} \tag{4}$$

where $\mathbf{W}$ is a set of arbitrary weighting functions. Considering that the analysis domain Ω is discretized into elements Ω^e, an approximation to the conservative variables vector $\mathbf{U}$ can be defined inside each element Ω^e using standard FE interpolation by $\mathbf{U}(x) = N_j \mathbf{U}(x_j) = N_j \mathbf{U}_j$ where N_j is the standard finite element shape function associated with the element node j and $\mathbf{U}_j$ is the value of $\mathbf{U}$ at the same node (note that the implicit summation convention has been adopted). Similarly, the flux vectors can be interpolated as $\mathbf{F}_k(x) \cong N_j \mathbf{F}_k(x_j) = N_j \mathbf{F}_k$. Then, the Galerkin variational formulation $(W_j=N_j)$ of Eq. (4) can be expressed for a generic node i (i = 1..n, with n being the number of nodes in the mesh) as follows

4

$$\int_\Omega N_i \left(N_j \frac{d\overset{\circ}{U}_j}{dt} + \frac{\partial N_j}{\partial x_k} \tilde{F}_k \right) d\Omega = 0 \qquad \forall i \in \Omega \tag{5}$$

and using matricial notation the latter becomes

$$\frac{d\overset{\circ}{U}_j}{dt} = \mathbf{M}^{-1}\mathbf{r}$$

$$\mathbf{M} = \int_{\Omega^e} N_i N_j \, d\Omega \tag{6}$$

$$\mathbf{r} = -\int_\Omega N_i \frac{\partial N_j}{\partial x_k} d\Omega \, \tilde{F}_k$$

where $\mathbf{M}$ is the standard FE mass matrix and $\mathbf{r}$ is the right hand side vector. To improve computational efficiency an edge data structure is adopted. An edge is defined by a pair of nodes sharing a common element. Let us denote by i and j the nodes of a given edge. The residual in (6) can be rearranged in the following manner

$$\mathbf{r}^i = -\sum_{j \neq i} \int_\Omega N_i N_{j,k} \, d\Omega \, \tilde{F}_k - \int_\Omega N_i N_{i,k} \, d\Omega \, \tilde{F}_k \tag{7}$$

in which $N_{j,k} = \partial N_j / \partial x_k$ and the sum extends to all values of j except i. The integration by parts of Eq. (7) yields

$$\mathbf{r}^i = \int_\Omega N_{i,k} N_j \, d\Omega \, \tilde{F}_k - \int_\Omega N_{i,k} N_j \, d\Omega \, \tilde{F}_k - \int_\Gamma N_i N_j n_k \, d\Gamma \, \tilde{F}_k - \frac{1}{2} \int_\Gamma N_i N_i n_k \, d\Gamma \, \tilde{F}_k \tag{8}$$

where $\tilde{F}_k = \tilde{F}_k + \tilde{F}_k$ is twice the interface (average value at the edge midpoint) flux and $\mathbf{n}$ is the normal outward vector at the boundary Γ. To achieve the full benefits of edge storage Eq. (8) is symmetrised in the following manner

$$\begin{aligned}
\mathbf{r}^i = {} & \frac{1}{2} \int_\Omega \left(N_{i,k} N_j - N_i N_{j,k} \right) d\Omega \, \tilde{F}_k + \int_\Gamma N_i N_j n_k \, d\Gamma \, \tilde{F}_k - \int_\Omega N_{i,k} N_j \, d\Omega \, \tilde{F}_k \\
& - \int_\Gamma N_i N_j n_k \, d\Gamma \, \tilde{F}_k - \frac{1}{2} \int_\Gamma N_i N_i n_k \, d\Gamma \, \tilde{F}_k
\end{aligned} \tag{9}$$

Then, using the shape function property $N_i = 1 - \sum_{j \neq i} N_j$, Eq. (9) can be expressed as

$$\mathbf{r}^i = d_k^{ij} \tilde{F}_k + b_k^{ij} \tilde{F}_k + c_k^i \tilde{F}_k \tag{10}$$

where

$$d_k^{ij} = \frac{1}{2} \int_\Omega \left(N_{i,k} N_j - N_i N_{j,k} \right) d\Omega$$

$$b_k^{ij} = -\frac{1}{2} \int_\Gamma N_i N_j n_k d\Gamma \qquad (11)$$

$$c_k^i = -\int_\Gamma N_i N_i n_k d\Gamma$$

Note that because the **d** coefficients are antisymmetric ($d_k^{ij} = -d_k^{ji}$) only half of them have to be stored; moreover, the **b** and **c** terms are zero for any interior edge. Consequently, storage requirements are greatly reduced when the edge representation is adopted. Furthermore, owing to the antisymmetric character of the **d** coefficients, it is possible to demonstrate that the numerical scheme given by Eq. (10) is conservative. Indeed, the total contribution to the residual due to any couple of internal nodes the is zero, i.e.

$$\mathbf{r}_e^i + \mathbf{r}_e^j = d_k^{ij} \mathbf{F}_k^{ij} + d_k^{ji} \mathbf{F}_k^{ji} = d_k^{ij} \mathbf{F}_k^{ij} - d_k^{ij} \mathbf{F}_k^{ij} = \mathbf{0} \qquad (12)$$

At times, the nodal values of the solution derivative are needed (be it for calculating the **G** terms in Eq. (1) if the full Navier-Stokes set is being solved or for obtaining the extrapolated interface values needed for convective stabilization, as indicated in the next section). When using linear elements a derivative recovery step is needed. Assuming the derivatives can be interpolated by the FE shape functions, nodal gradients can be obtained through a smoothing procedure as follows

$$\int_\Omega N_i N_j d\Omega \nabla_k \mathbf{U}^j = \int_\Omega N_i N_{j,k} d\Omega \, \mathbf{U}^j$$

$$\nabla_k \mathbf{U}^j = \mathbf{M}^{-1} \int_\Omega N_i N_{j,k} d\Omega \, \mathbf{U}^j \qquad (13)$$

In (6) and (13) a linear system of equations must be solved. Under many circumstances an approximate solution using the diagonal mass matrix is acceptable. In such cases the consistent mass matrix in (6) is replaced by its lumped counterpart given by

$$\mathbf{M}^d = \delta_{ij} \sum_j \int_\Omega N_i N_j d\Omega \qquad (14)$$

Whenever the consistent matrix must be employed a very efficient solution strategy is to use the iterative scheme

$$\mathbf{M}^d \left. \frac{d\tilde{\mathbf{U}}}{dt} \right|_0 = \mathbf{r}$$

$$\mathbf{M}^d \left(\left. \frac{d\tilde{\mathbf{U}}}{dt} \right|_m - \left. \frac{d\tilde{\mathbf{U}}}{dt} \right|_{m-1} \right) = \mathbf{r} - \mathbf{M} \left. \frac{d\tilde{\mathbf{U}}}{dt} \right|_{m-1} \tag{15}$$

this algorithm usually yields a very accurate solutions after only three iterations.

2.3 Convective stabilization

As the basic Galerkin discretization is inherently unstable in presence of large convective fluxes, the numerical scheme presented in the previous section is prone to spurious oscillations which render it completely useless. Consequently, some dissipation terms must be introduced in order to provide the necessary stabilization for the scheme. This can be achieved by replacing the interface fluxes $\mathbf{F}^{ij}$ by new numerical fluxes where numerical dissipation is introduced in an explicit manner or the fluxes are modified according to the physics of the problem. In this work the numerical fluxes are calculated using Roe's approximate Riemann solver [3] which leads to

$$\tilde{\mathbf{F}}_k^{ij} \rightarrow \mathbf{F}_k^{ij} = \tilde{\mathbf{F}}_k^{i} + \tilde{\mathbf{F}}_k^{j} - \frac{1}{2} \left| \mathbf{A}_{\mathbf{u}^{ij}} \right| \Delta^{ij} \, \mathbf{u}_k^{ij} \tag{16}$$

where

$$\mathbf{u}^{ij} = \frac{\mathbf{l}^{ij}}{\left\| \mathbf{l}^{ij} \right\|} \quad , \quad \mathbf{l}^{ij} = \mathbf{x}^j - \mathbf{x}^i \quad , \quad \Delta^{ij} = \tilde{\mathbf{U}}^j - \tilde{\mathbf{U}}^i \tag{17}$$

and $\left| \mathbf{A}_{\mathbf{u}^{ij}} \right|$ is the positive flux Jacobian matrix evaluated along the direction of the edge $\mathbf{u}^{ij}$. Replacing the interface fluxes in Eq. (10) by the numerical fluxes from (16) a monotone low order scheme is obtained. In order to recover a higher order spatial accuracy in regions where the flow is smooth, the amount of dissipation is reduced replacing the nodal conservative variables in Δ^{ij} by high-order extrapolations at the edge interface, i.e.

$$\mathbf{F}_k^{ij} = \tilde{\mathbf{F}}_k^{i} + \tilde{\mathbf{F}}_k^{j} - \frac{1}{2} \left| \mathbf{A}_{\mathbf{u}^{ij}} \right| \left(\tilde{\mathbf{U}}^{j-} - \tilde{\mathbf{U}}^{i+} \right) \mathbf{u}_k^{ij} \tag{18}$$

The extrapolated values of the conservative variables at the interface $\tilde{\mathbf{U}}^{j-}$ and $\tilde{\mathbf{U}}^{i+}$ are obtained by means of a limited MUSCL scheme [4] using the recovered nodal gradients from Eq. (13) in order to carry out the extrapolation.

2.4 Time discretization

The temporal discretization of Eq. (6) is done in a fully explicit manner by means of a multi-stage Runge-Kutta scheme. The allowable local time step is calculated by means of the

following expression

$$\Delta t_i = C \frac{h_i}{\|\mathbf{u}^i\| + a^i} \qquad (19)$$

where C is the Courant number, a^i the speed of the sound and h_i is a representative nodal size. The nodal size is taken as the minimum height of all the elements containing node i. This choice of size minimizes convergence problems when the grid contains highly distorted elements. In order to accelerate the solution convergence to the steady state an implicit residual smoothing is performed before solving. This is accomplished by

$$\bar{\mathbf{r}}^i = \mathbf{r}^i + \varepsilon \sum_j \left(\bar{\mathbf{r}}^j - \bar{\mathbf{r}}^i \right) \qquad (20)$$

where the sum extends to all j connected to node i. The equation above is solved using a few Jacobi iterations as follows

$$\bar{\mathbf{r}}_n^i = \frac{\mathbf{r}^i + \varepsilon \sum_j \bar{\mathbf{r}}_{n-1}^j}{1 + \varepsilon \sum_j 1} \qquad (21)$$

3. THE AERODYNAMIC MODEL

The analysis geometry involves a wing-body-tail (WBT) test model configuration supported by a twin-sting mounting arrangement. The shape corresponds to a modern large jetliner. The 1:50 scale model has a half-span of 79cm. In the present work three different support configurations have been analyzed in order to evaluate their effect on model deformation. These shall be referred to, from now on, as outboard, intermediate and inboard boom positions. The respective sting spacings are 43, 35 and 30 inches, corresponding to 69%, 56% and 48% spanwise positions (the choice of values in the British system is due to historical reasons related to the manufacture date of parts of the support mechanism). All of them have been tested using the Standard Twin-Sting Rig (STSR) during the ARA test campaign. The intermediate spacing was also tested at ETW using the Enhanced Twin-Sting Rig. The outermost boom position was chosen based purely on the allowable material stresses and is meant to provide an upper limit on the aeroelastic deformations. The intermediate position is representative of standard practice and, finally, the smallest boom spacing was selected in order to gain understanding on the interference effects on the empennage caused by the twin-sting arrangement. Due to the fact that flow conditions and geometry are symmetric with

respect to the aircraft symmetry plane (x-z), a half-symmetric computational model is used. Figure Fig. 1 shows the test model geometry and the different sting positions studied here.

Fig. 1: Test model showing the three boom spacings tested.

As the picture shows, the full assembly of the wind tunnel support system has not been modelled (the yoke plate and boss have been removed). In order to simplify the geometry, only the stings have been considered. The rear part of the booms has been streamlined to minimize the disruption of the flow pattern. The resulting computational model offers substantial savings in both, meshing effort and CPU-runtime requirements. An unstructured tetrahedral mesh, containing approximately ten million elements, has been generated from the STSR and test-model CAD geometries. Figure Fig. 2 shows a detail of the CFD surface mesh around wing-boom adaptor area.
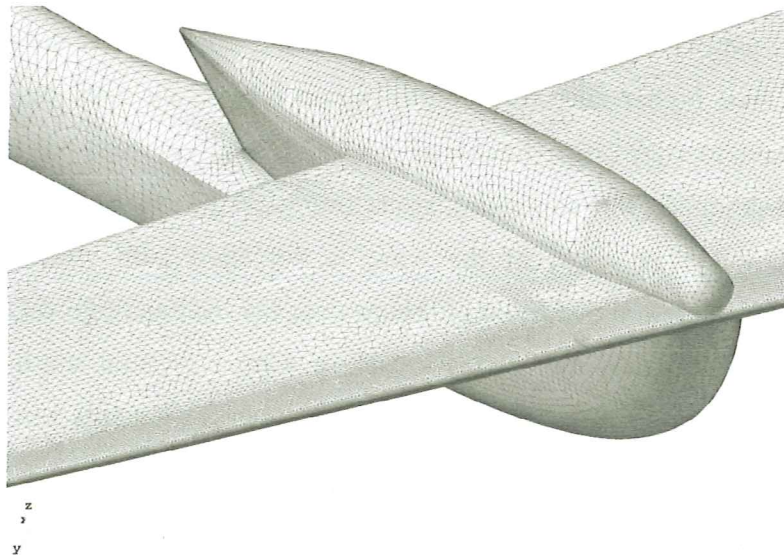
Fig. 2: Detail of the CFD surface mesh in the wing-boom adaptor area.

As it has been mentioned before, this work focuses on the assessment of wing deformations caused by the twin-sting rig. Analyzing the relative magnitude of the different aerodynamic

forces acting on the model during the wind tunnel tests, it can be observed that the modulus of the viscous shear stresses acting on the wing is small compared with the pressure differences encountered. Moreover, the wing bending moment caused by the viscous stresses acts approximately around the model z-axis, the direction for which the wing bending stiffness is highest. Consequently, it can be safely assumed that most of the wing structural deformation is caused by the pressure field with viscous forces playing a negligible role. Hence, the fluid has been considered inviscid allowing for considerable computational savings (for the flight regimes analyzed no large separation areas appear, so the Euler equations provide a good approximation to the real flow field).

4. THE STRUCTURAL MODEL

An overview of the structural modelling of the WBT configuration, the support system and the fluid-structure coupling procedure adopted is presented next.

4.1 The wing structural model

A 3D FEM model of the wing structure has been developed in order to asses the changes in wing twist and bending caused by the twin-sting mounting arrangement. For structural modelling purposes, the wing has been considered to be solid as the internal cavities necessary to accommodate the measuring equipment do not produce significant changes in the stiffness of the structure. If the highest level of accuracy is sought in the calculations, a structural mesh containing only well-shaped hexahedral elements should be used. However, this is difficult to achieve using only brick-type elements, specially on the area surrounding the leading edge. The higher curvature of this region (especially near the wing tip) would cause some elements to warp beyond acceptable levels. To circumvent this problem a hybrid mesh, hexahedral-dominant but containing some triangular prisms on the leading edge, has been adopted. In this way, most of the wing is modelled with well-shaped structured hexahedral elements while the distortion problems near the leading edge are alleviated by the prismatic elements. Following this methodology, a wing structural mesh contains 49358 nodes shared by 6160 prisms and 40000 brick (hexahedral) elements has been generated. Figure Fig. 3 shows the top and side views of the wing structural mesh.
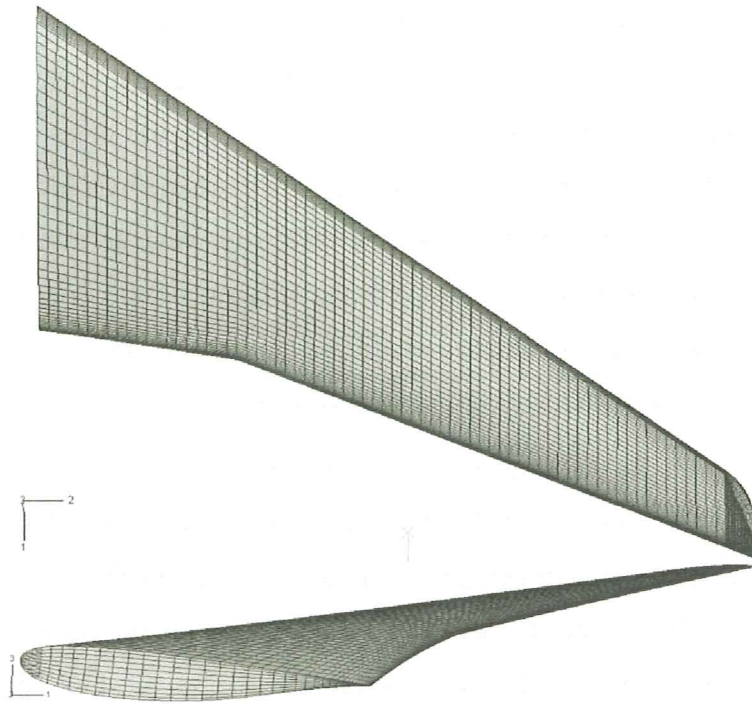
Fig. 3: Top and side views of the structural wing mesh.

Fully integrated linear elements subject to bending tend to show an overly large stiffness due to their inability to reproduce a linearly varying strain field without developing parasitic shear stresses [7]. Thus, it would be advisable to use second order elements to avoid shear locking problems. Unfortunately, as the wing section tappers towards the tip the elements become severely skewed (especially at the leading edge, as it curves backwards over a very short distance). Second order elements suffer considerable performance degradation under these circumstances and can lead to severe convergence problems (caused by the Jacobian of the isoparametric transform becoming negative). To overcome this difficulty, it was decided to employ first order (linear interpolation) elements, as their behaviour is less sensitive to distortion. To prevent the mesh from developing shear locking, enhanced strain field linear elements have been used. These elements include additional incompatible displacement modes that prevent spurious shear stresses. To double check the results, tests have also been performed using reduced integration elements which do not suffer from shear locking (as no strain develops at their integration points when subject to pure bending). Reduced integration elements have been used together with hourglass control to prevent the development of zero-energy modes that would invalidate the results. No differences in behaviour have been observed between the two element formulations so the results can be considered reliable.

4.2 Support mechanism modelling

Large vertical displacements along the model z-axis and rotations along the y-axis (spanwise direction) are to be expected due to the bending deformation of the sting booms. The effects of rigid body displacements of the supporting mechanism on the measurements carried out during testing are quite limited because model attitude is measured via inclinometers mounted on the fuselage. However, there is an important effect on wing deformation caused by the torsional stiffness of the booms, as it restricts the rotation of the wing around the x-axis (fuselage direction) and therefore hampers bending deformation. This fact has to be properly accounted for if accurate deformations are to be predicted.

The stings have been modelled using beam elements whose bending and torsional stiffness have been calculated from the detailed CAD geometry provided by ARA. As the dynamic pressure at the test chamber during the ARA campaign was relatively low (compared to ETW runs) the displacements caused by the flexibility of the yoke plate can be neglected. Therefore, only the effect of the booms is accounted for in the FEA model. Given their general proportions, the wing-boom adaptors have been replaced by a rigid body as their stiffness is much higher than that of the booms. The realistic simulation of the adaptor-wing junction would require a very detailed modelling of the attachment mechanism to produce an accurate rendering of the stress field around the load transfer area (including for example information about the bolt adjustment torque). To avoid unnecessary complexity, the model has been simplified in this area. The load from the adaptors has been transferred to the wing by rendering a group of elements around the fasteners extremely rigid and constraining their movements to those of the adaptor. In this way, the load transfer is spread out over several elements producing a locally smooth deformation field.

4.3 Body-tail section modelling

As the deformations sought are those of the wing, the computational complexity has been reduced by removing the body-tail assembly from the structural mesh. To this effect, the overall pressure force and moments acting on the surface have been calculated and referred to a single reference point situated at the symmetry plane, next to the wing root (shown in Fig. 4). Hence, the effects of the body-tail group are accounted for without increasing the number of degrees of freedom of the model.
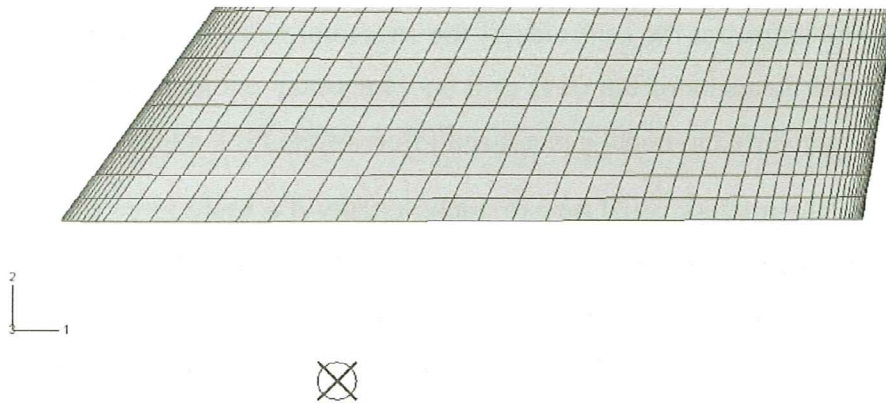
Fig. 4: Position of the body-tail load reduction point (crosshair inside circle).

4.4 Modelling of the body-wing interface

The load transfer mechanism at the wing root depends on the geometrical details of the junction as well as on the fastening system used. In this work a simplified model has been adopted for the wing-body interface. A group of elements on the upper and lower sides of the wing root (six along each) has been lumped into a single rigid body whose master reference node (the node to which the displacements of all the nodes in the rigid body are tied to) is the reduction point of the fuselage-tail assembly. In this way, the rotation of the wing root section is kept to zero in relation to the fuselage while a certain level of warping is allowed (fully constraining the warping of the section could give rise to an unrealistic torsional stiffness at the wing root). Note that this form of attachment can be considered as being similar to spot-welding the wing root to the fuselage body. Furthermore, x-z symmetry conditions for the model are enforced constraining the motion of the body-tail reference node along the y-axis as well as the rotations about the x and z-axes. In this way, the effects of the body-tail on the wing are reproduced in a very cost-effective way.

4.5 Transfer of the aerodynamic loads to the structural model

An automated method to map the pressure distribution from an arbitrary CFD grid into the FEA mesh has been developed. This load transfer procedure is carried out in four main steps:

1. The CFD surface mesh is split in two groups, the first one containing elements belonging to the body-tail area and the second one including all the remaining surface facets.

2. The pressures acting on the body are reduced to a global force and moment acting on the reference point.

3. For each surface facet of the structural grid, the centroid is calculated and the element of the CFD mesh it lays on is sought.

4. The average pressures at the centroids of the structural mesh facets are interpolated using values from the elements of the CFD grid on which they are located. These pressures are subsequently converted to nodal generalized forces of the FEA model.

The third step of the process could be extremely lengthy if a brute force approach were used to find the correspondence between the CFD and the structural grids. For a CFD grid containing n_c facets and a FEA surface mesh having n_s elements, a total of $n_c \times n_s$ checks would have to be performed. It is clear that this is an extremely inefficient process which calls for improvement. To achieve this, a *binning* algorithm has been implemented [5]. A background, uniformly spaced, hexahedral structured mesh is created which encompasses the complete wing. In a first step, the CFD facets are assigned to the elements of the background mesh (the bins) according to the position of their centroids. Given the uniform spacing of the bins, the parent bin of any point can be located by simply operating on its coordinates and the process is thus extremely fast. In a second step, the underlying fluid element of each structural face is found by searching only across the elements belonging to the same bin. The cost of the search is then reduced by a factor equal to the number of elements on the background mesh. As the number of bins can be made as large as needed, the speed-up attained is quite remarkable.

4.6 Coupling procedure

The pressure distribution obtained from the CFD solution is converted to nodal generalized forces applied on the FEA model but the displacements and rotations thus obtained are not used to deform the aerodynamic model and recalculate the pressure forces. No iteration between the CFD and the structural model is performed and, consequently, the static aeroelastic equilibrium of the wing is not achieved. As the structure of the test model is very stiff the total displacements are generally small so neglecting the effect of the deformations on the flow field does not lead to severe errors. To validate this assumption a cross-check has been made against experimental deformation data gathered at ETW. Using Image Pattern Correlation Technique (IPCT) and Stereo Pattern Tracking (SPT) displacement measurements were carried out. Both techniques are based on photogrammetric principles [6]. In SPT a regular array of spot markers are tracked while IPCT relies on randomly sprayed paint droplets.
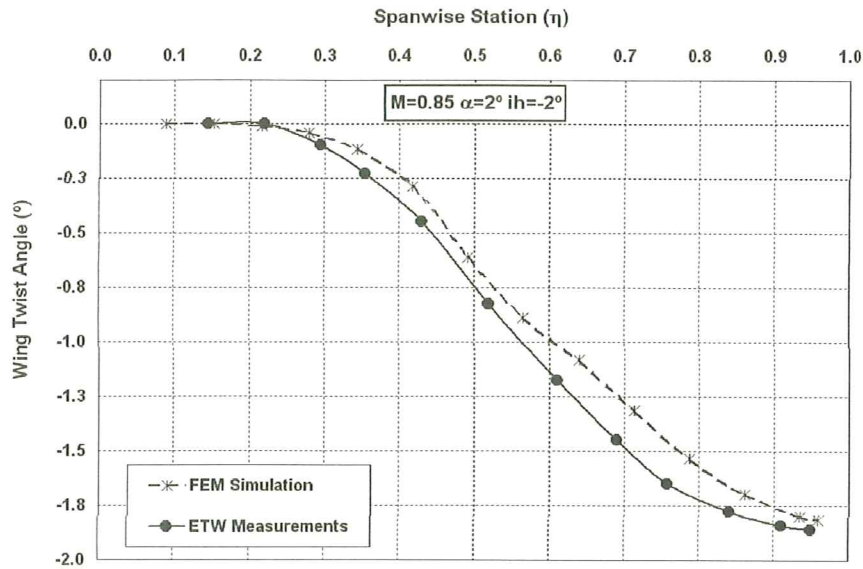
Fig. 5: Simulated vs experimental wing twist. $M_\infty = 0.85$, $\alpha = 2°$, Mid boom position, HTP incidence setting = -2°.

The good agreement between the numerical and experimental results is shown in Fig. 5. The general trend as well as the actual rotation values are well captured. I must be stressed that the differences seen on the graph are not significant. During ETW test runs discrepancies on the order of 0,15° were observed between the SPT and IPCT measurements. Thus, the differences in Fig. 5 may well be caused by experimental uncertainties. The *one-way coupling* procedure adopted in this work seems therefore very accurate.

5. WING DEFORMATION ANALYSIS

In this section the influence of the freestream Mach number and the angle of attack on wing deformation is analyzed for each support arrangement mentioned in Section 3. The flow conditions studied in this work involve Mach number values ranging from 0.35 to 0.95 and incidence angles between $\alpha = -2°$ and 3.4°. In order to transform the Cp values obtained from the CFD solution into pressure loading, a constant stagnation pressure of 1bar is assumed to match the test chamber conditions encountered during the ARA wind tunnel runs. The mechanical properties of the model material are a Young's modulus of 181GPa and a Poisson's ratio of 0.3.

To assess the effects of the mounting system on wing deformation, two deformation parameters have been investigated. The first one is the rotation angle about the y-axis of the wing sections (also termed twist angle). This parameter is considered to be the most relevant results from the structural analysis because it represents the local change in angle of attack due to aeroelastic effects and has a major impact on the downwash distribution at the tail. For

15

each of the cases under study, the twist angle has been computed at several spanwise stations in the following manner

$$\text{twist angle} = \tan^{-1}\left(\frac{u_z^{LE} - u_z^{TE}}{x^{LE} - x^{TE}}\right) \quad (22)$$

where u_z^{LE} and u_z^{TE} respectively denote the vertical displacement of points located at the leading x^{LE} and the trailing edge x^{TE} of each wing section where the twist angle is computed. Moreover, the fuselage rotation has been subtracted from the results given by Eq. (22) forcing the computed twist to be zero at the wing root section. The second parameter under study is the vertical displacement of the wing (along z-axis). This value is provided mainly for reference purposes, as it is not so important from the point of view of aerodynamic interference (its effect in downwash is limited). The quarter chord line is adopted as a reference for plotting the vertical displacements given its special importance in aerodynamics. It should be noted that the deformations presented in this work are only due to aerodynamic forces as the contribution of the model weight has not been accounted for. To evaluate the mechanical effect of the STSR on wing deformation, a limited number of structural runs without booms (booms-off) have been performed. For these computations the wing has been supported by clamping its root section reference node. It must be remarked that the pressure field in these runs is the same as in the computations including the stings (booms-on) thus reflecting only the mechanical effect of the suspension system (aerodynamic interference is not accounted for). The most relevant obtained for the different test cases analyzed are presented in the next section.

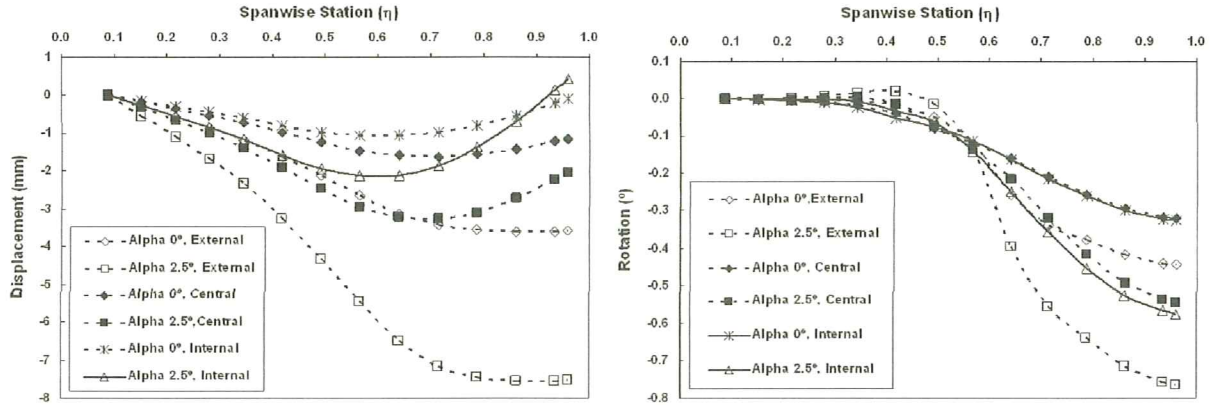## 5.1 Effect of the sting boom position on wing deformation

The effects of the STSR on both wing vertical displacement and rotation computed for a freestream Mach number $M_\infty = 0.85$ are presented in Figure 5. Note that the displacement pattern inboard of the wing-boom adaptors is reversed with respect to the situation when the model is supported by the fuselage as a downward reaction at the booms is needed to counteract the lift force acting on the test model. Thus, the wing root-section rises relative to the boom area and outboard from the latter the usual behaviour is recovered; i.e. the upward vertical deflection increases toward the wing tip.
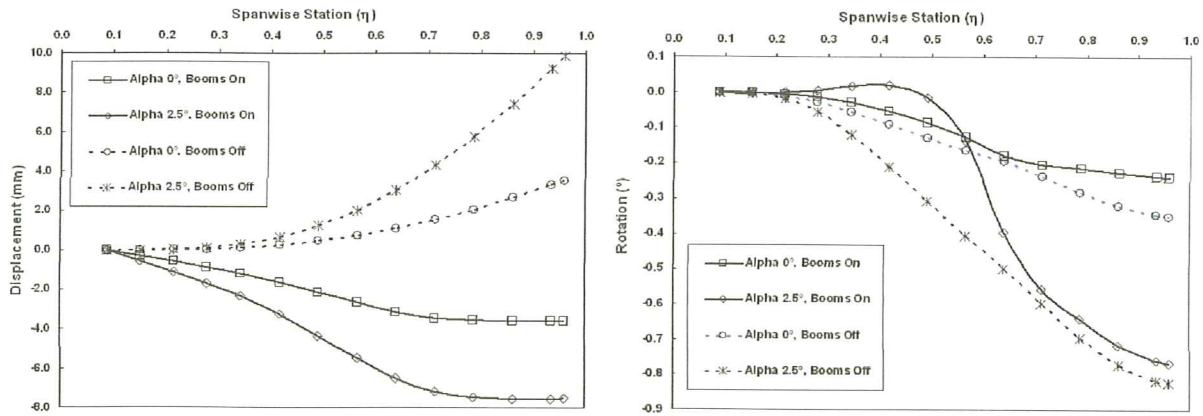
Fig. 6: Effect of support mechanism and incidence angle on wing deformation. M∞= 0.85. Outboard boom position.

Figure Fig. 6 shows that the twist angle steadily decreases from the root to the wing tip for the booms-off condition. This is to be expected due to the positive sweep of the wing. The twin-sting support alters this behaviour causing the twist angle to increase near the wing root; as the angle of attack increases this trend becomes more pronounced. The absolute value of twist at the wing tip observed for the booms-on configuration is smaller than the value attained when the model is supported trough the fuselage. This behaviour can be explained as follows. When the angle of attack increases, the upward lift force originated at the HTP grows, causing an additional nose-down (negative) moment on the fuselage. This pitch unbalance must be compensated by the sting booms, which react with an opposite torsion moment producing a nose-up (positive) rotation of the wing-sections inboard of the adaptors. On the other hand, due to the backward sweep of the wing, the upward bending deformation due to the spanwise lift distribution causes a negative twist which counteracts the effect of torsion due to the booms. Close to the wing root the positive rotation due to the adaptor moment dominates (also, in that area the vertical displacement pattern is reversed, so bending deformations do not lower the local angle of attack) causing the twist angle to increase initially. Moving further outboard, the effect of boom torsion vanishes (as the outer section of the wing is only subject to the aerodynamic loads with the adaptors having no effect) and the usual booms-off trend is recovered. Despite the important differences in the twist pattern, the overall wing twist is reduced by the STSR. This support technique does not seem to be inferior to other conventional mounting systems if only the absolute magnitude of the shape change is considered. In order to achieve definite conclusions, certain additional factors, such as the stresses to which the model is subject, should be taken into account but these fall outside the scope of this work.

The influence of sting spanwise position on wing deformation is studied comparing results for the outermost, intermediate and innermost sting configurations and the results are presented in Fig. 7. As expected, numerical calculations predict larger deflections when the supports are placed farther away from the symmetry plane.

**Fig. 7**: **Sting boom spanwise position effects on wing deformation. $M_\infty = 0.85$, $\alpha = 0°$ and 2.5°.**

As it has been mentioned before, downward deflections occurs inboard of the wing-boom adaptor whereas the usual upward displacement is observed for the outboard wing stations. The overall wing deflections are smaller when the stings are located near the symmetry plane. Except for the innermost adaptor position, the deflections across the outboard section are smaller than the displacements encountered inboard of the booms. As far as the magnitude of the displacements is concerned, the STSR mounting is no worse than the standard test setup. This can be checked in Fig. 6 where a worst case scenario (the widest boom spacing) is compared with the booms-off configuration. While there is an evident change on the deformed shape, the geometrical changes are smaller for the booms-on configuration.

The effect of boom spanwise position on the local rotation angle is also shown in Fig. 7. It can be observed that the behaviours obtained for the inboard and the intermediate adaptor positions are quite similar. The relative proximity of the two innermost adaptor positions and the large stiffness of the wing section near the root could account for this result. However, the differences encountered for the outermost setting are important. In this case, the wing is attached at a section of lower stiffness farther apart from the symmetry plane and, consequently, the effects of torsion become stronger.

5.2 Effect of the angle of attack

An increment of the angle of attack gives rise to a higher wing loading which, in turn, increases the vertical spanwise displacements. The local rotation angle is also affected in a similar way, though to a lesser degree. As explained before, this is due to the change in HTP

lift which takes place (as the test model is not trimmed) and causes a positive wing twist inboard the adaptors. These behaviours are more pronounced for the outer wing-boom adaptor position as the distance between the supporting stings is larger. Fig. 8 shows the effects of the angle of attack for the outer sting configuration computed for a Mach number $M_\infty=0.85$.
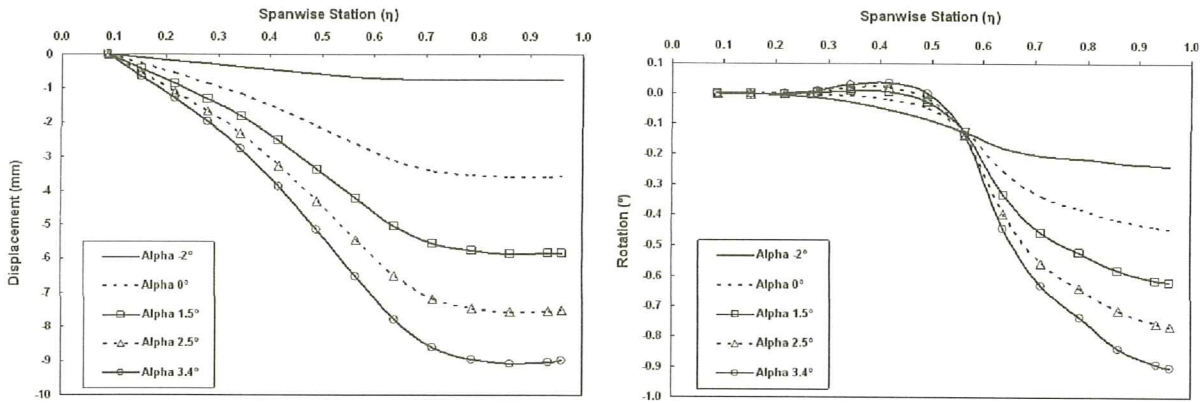

Fig. 8: Effects of the angle of attack on wing deformation. Outermost boom position, $M_\infty = 0.85$.
Observe that close to the wing root the twist plots change very lightly with the angle of attack because the pitch-down moment due to the HTP compensates for the increased wing loading. It is possible to observe at the spanwise station $\eta = 0.55$ that the rotation angle is insensitive to changes in the model incidence and remains almost constant.
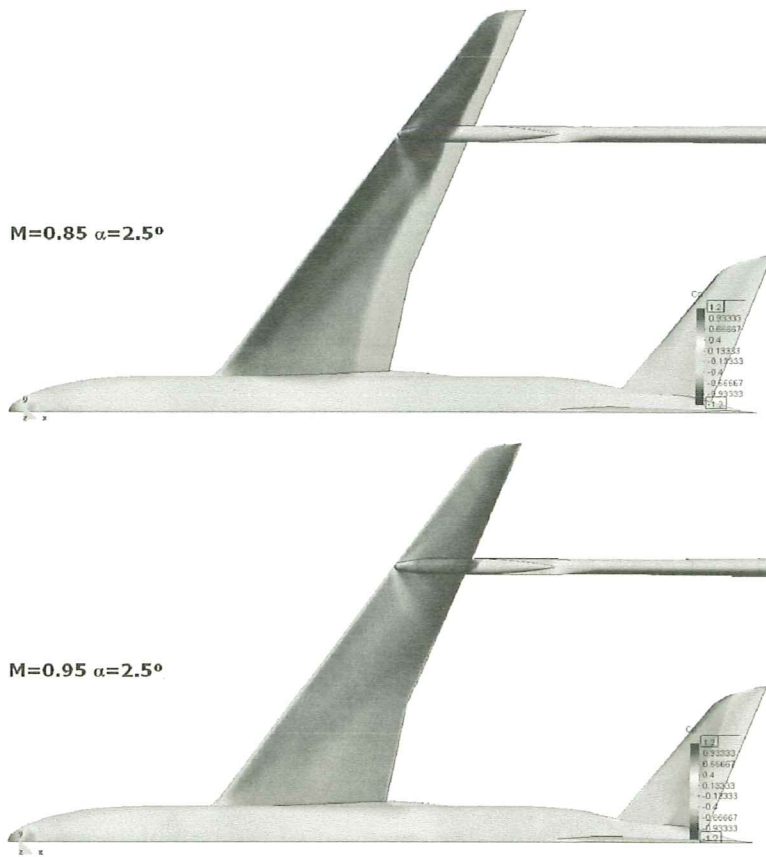
5.3 Effect of the Mach number

A large increase in the wing deflection occurs when the Mach number is augmented, which can be observed in Fig. 9. This is mainly a result of the experimental procedure followed. As the stagnation pressure inside the test chamber was kept constant during the ARA runs, the absolute value of the pressure differences acting on the model shows a strong dependence on the Mach number. Even though the pressure coefficient itself is also a function of the Mach number, when the Cp values are transformed into pressure loading for the structural model the change in dynamic pressure becomes the dominant factor. The enormous difference between the plots obtained for $M_\infty=0.35$ and $M_\infty=0.85$ in Fig. 9 clearly illustrates this effect. ETW test runs were less prone to this kind of behaviour due to the fact that a tighter control on the dynamic pressure was possible.

19
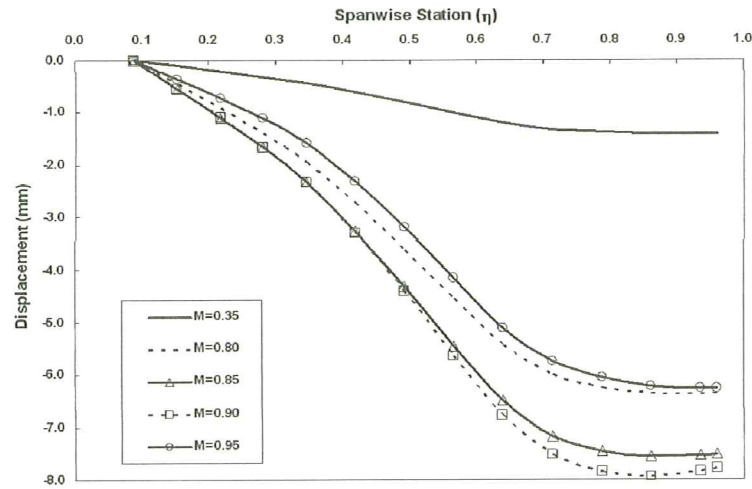
Fig. 9: **Mach number effects on the wing vertical displacements. Outer boom position and $\alpha = 2.5°$.**

Note that the wing deflection decreases appreciably for the highest value of the Mach number, i.e. $M_\infty = 0.95$. This is due to the poor aerodynamic behaviour of the wing under such extreme off-design conditions (lift divergence). Fig. 10 shows the pressure distribution on the model for Mach number values of $M_\infty = 0.95$ and 0.85. The decrease in lift when moving from Mach number 0.85 to 0.95 is quite remarkable (note that even though the size of the suction area increases, the magnitude of the pressure coefficient over the wing upper surface is greatly reduced, resulting in a smaller lift force). The same anomalous behaviour at $M_\infty = 0.95$ can be observed in the wing twist distribution presented in Fig. 11. Due to the reduced wing deflections, the twist due to wing sweep angle decreases. In addition, as can be seen in Fig. 10, the HTP lift distribution is not disrupted to such a large extent. Therefore, the positive wing twist introduced by the support mechanism does not decrease noticeably when the Mach number is increased. In this situation, the overall effect is an increased positive twist inboard of the booms adaptors accompanied by a lowered negative twist on the outboard sections. Thus, except for the mid-span section where the torsional effect of the booms is dominant, the curve corresponding to $M_\infty = 0.95$ shows the smallest values of twist across the entire transonic range (in spite of the changes in dynamic pressure due to the experimental setup).

20

M=0.85 α=2.5°

M=0.95 α=2.5°

Fig. 10: Cp distribution. Outboard boom configuration, α = 2.5°.
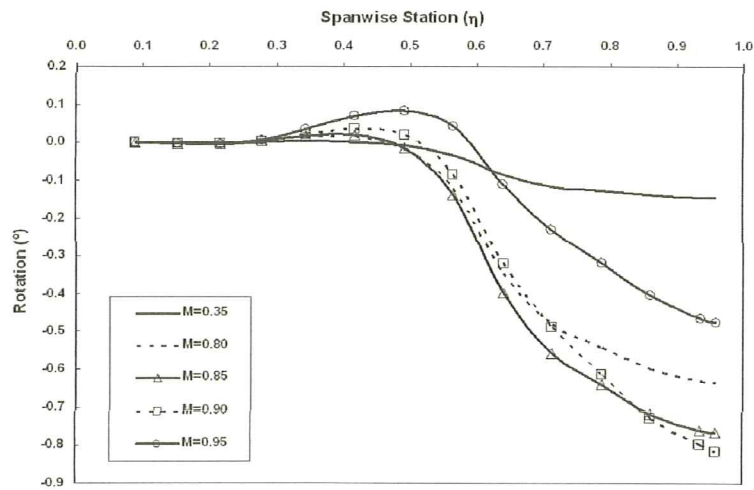

Fig. 11: Mach number effect on wing twist angle. Outer boom position, α = 2.5°.

5.4 Global effects of the STSR on wing deformation

With the aim of giving a better understanding of the effects of the STSR on the wing, its deformed shape is drawn for both the booms-on and booms-off configuration in Fig. 12. The differences in the iso-displacement lines computed for both cases are quite apparent.

Outer-boom position　　　　Boom-off
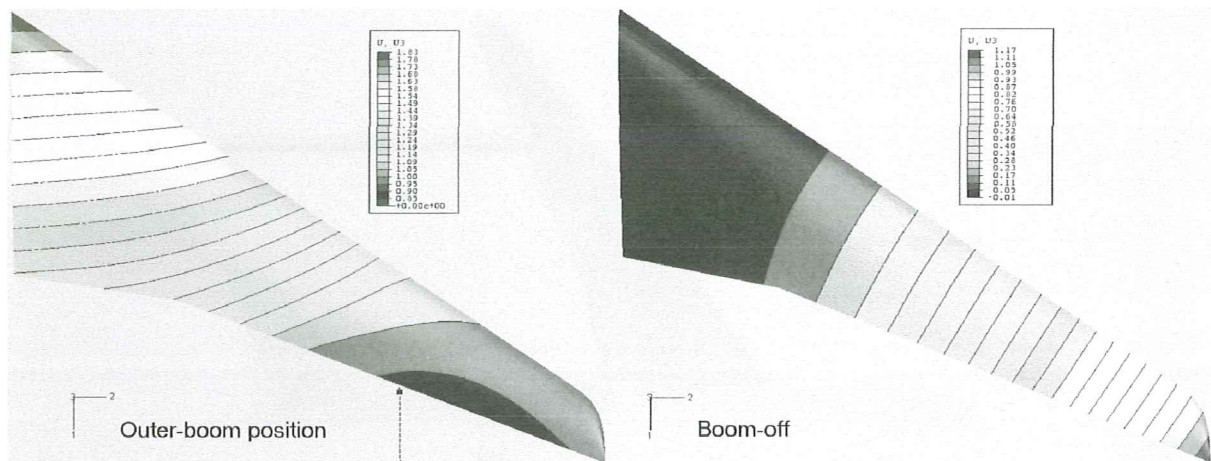
Fig. 12: Vertical displacements along the wing (cm). $M_\infty = 0.85$, $\alpha=2.5$.

For the booms-off configuration the displacement isolines are approximately perpendicular to the mid-chord line (more precisely, to the elastic axis of the wing). However, when the sting is attached to the wing, the displacement pattern is vastly different. Notice that near the wing root the lines are perpendicular to the fuselage, which indicates most of the displacement field corresponds to a rigid body motion of the fuselage. Most of this motion is due to bending of the booms (which causes a rigid body displacement of the complete model, wings included). There is also a displacement contribution arising from wing deformation, but it is much smaller. Slightly further outboard the lines curve towards the leading edge creating a motive which is somewhat similar to the free wing configuration. However, once the wing-boom adaptor area is reached the deformed shape changes abruptly. The boom stiffness restricts the rotation of the wing sections and the vertical displacement field over the outboard wing region becomes almost constant.

Figure Fig. 13 shows frontal views of the deformed wing computed for both configurations. The lift force generated by the inboard wing section tries to raise the fuselage when the sting booms are present and this upward force is countered by the downward reaction of the booms. Thus, the bending moment acting over the inboard section of the wing is reversed with respect to the booms-off configuration. Note that while the effect is readily apparent on the vertical displacements, the reversal effect is much less pronounced on the wing twist distribution. In the cases studied, twist reversal has been observed only for the widest boom spacing and, even when it takes place, the maximum positive twist is smaller than the absolute value of the negative twist that appears at the wing tip (see for instance Fig. 6).

22
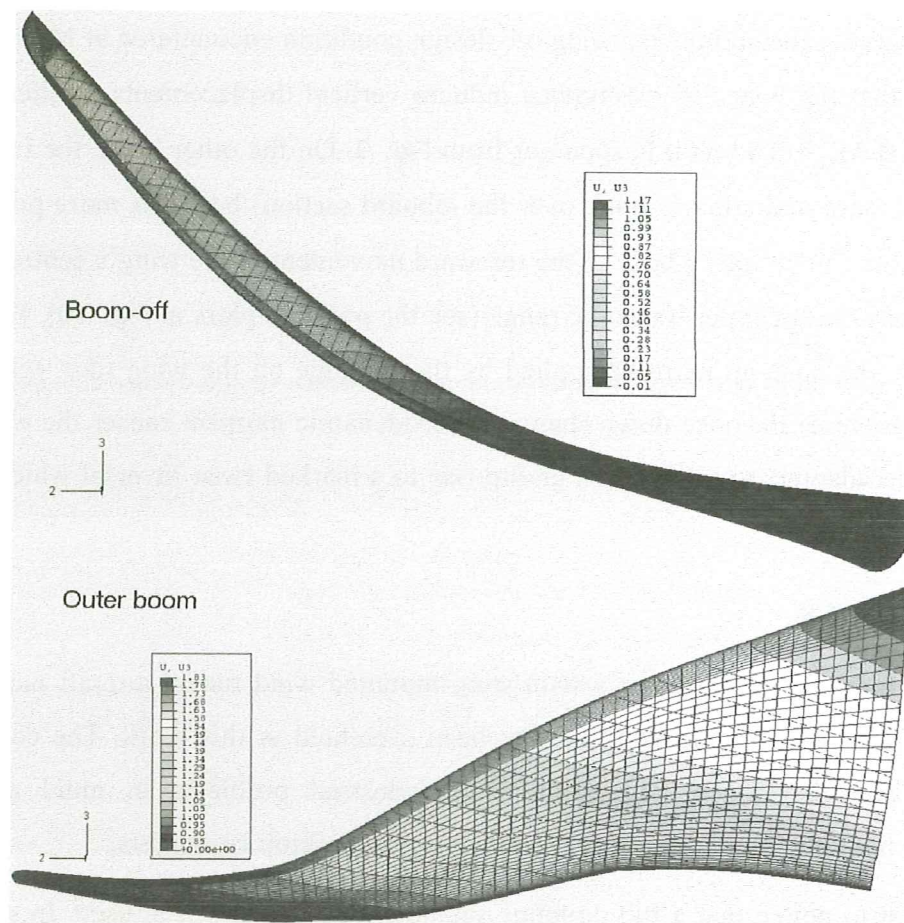
Fig. 13: Vertical wing displacements (cm). Displacement scale factor = 30. $M_\infty = 0.85$, $\alpha=2.5$.

As explained before, the positive rotation due to wing bending (which affects the region inboard of the wing-boom adaptors) is countered by the torsion caused by the HTP lift. The vertical force acting on the HTP can be large as the test model is not trimmed. When the test model is set at a low incidence angle the net force acting on the tail is negative (downward) and the fuselage introduces a nose-up moment on the wing root section. Thus, the sting booms have to compensate by introducing a negative moment along the y-axis (spanwise direction) which causes a negative twist. The two competing effects (torsion and bending) partially cancel each other resulting in an almost flat twist plot inboard of the wing-boom adaptors (Fig. 8 illustrates this behaviour). Once the angle of attack is increased, the tail downward force is decreased while the positive twist due to wing bending increases as a result of a higher wing load. Thus, the twist reversal phenomenon is most pronounced at high incidence settings (in fact, it disappears when the angle of attack is negative, see Fig. 8). As it was previously mentioned, there is no mechanical effect of the boom outboard of the wing-boom adaptor and only aerodynamic interference can modify the response relative to the booms-off configuration.

Finally, concerning the anomalous wing off-design condition encountered at $M_\infty = 0.95$, it has been shown that the wing lift divergence induces vertical displacements smaller than those encountered at $M_\infty = 0.85$ as it is apparent from Fig. 9. On the other hand, the twist reversal (spanwise increase in angle of attack over the inboard section) becomes more pronounced at $M_\infty = 0.95$. This can be traced back to the rearward movement of the wing's centre of pressure that takes place on the upper transonic range (see the pressure plots in Fig. 10). HTP lift and, consequently, the nose-up moment applied by the fuselage on the wing root, remain almost unaffected. However the nose-down change in aerodynamic moment causes the wing sections inboard of the adapters to pitch down giving rise to a marked twist reversal which is evident in Fig. 11.

6. CONCLUSIONS

The wing deformation analysis of a twin-sting-mounted wind tunnel aircraft model, mainly focusing on wing torsion and bending, has been presented in this work. The computational tools have been developed with large scale industrial problems in mind and a good performance has been obtained running exclusively on desktop computers.

It is important to notice that a full coupling methodology has not been used. In spite of this, the *one-way coupling* procedure developed here seems to be accurate enough for assessing the wing aeroelastic behaviour according to the objectives of this research. Experimental evidence corroborates the accuracy of the results. What is more, in the vast majority of cases the net effect of twist deformations is to reduce the local angle of attack, thus the geometric changes on the real test model are not expected to be larger than those predicted here (as wing load is reduced due to the deformation). Hence, the deformations calculated can be considered a realistic bound of the real ones.

From the data presented we can conclude that, inside the range of parameters analyzed in this work, the global deformations due to the twin-sting mounting system are not higher than those expected when a conventional single sting support system is employed (booms-off configuration). While there is an evident change on the deformed wing shape, the wing displacements and rotations computed for the three boom position are smaller than those calculated for the booms-off configuration. As least for the geometries analyzed here the initial fears of increased torsional deformations have been proven unfounded. Even the widest boom spacing, chosen specifically to generate larger-than-usual changes in geometry is no

different in this respect. While it yields displacements larger than the other two spacings, these are still smaller than for the booms-off case.

The differences in wing deformation pattern encountered between the booms-on and the booms-off configuration are noticeable. Thus, the variation of wing displacements and twist angle should be accounted for if tests with both single and twin-sting mounting systems are planned on the same model. Concerning structural integrity of the model, some extra requirements have to be met in order to avoid exceeding the load bearing capacity of the wing (especially for the wider boom spacing) but these fall out of the scope of this paper. In view of the results obtained it can be concluded that the choice of boom spacing should be based *fundamentally on the acceptable level of aerodynamic interference on the tail and the* structural integrity of the test model. The changes in shape seem to be of secondary relevance.

ACKNOWLEDGEMENTS

REFERENCES

[1] Abbas A., Dias J., Cabello J. REMFI Rear-fuselage and empennage flow investigation. CEAS-KATnet Conference, Bremen 2005.

[2] PUMI: An explicit 3D unstructured finite element solver for the Euler equations. R. Flores, E. Ortega. CIMNE Technical report, 2009.

[3] Roe P. L. Approximate Riemann solvers, parameter vectors and difference schemes. *Journal of Computational Physics*, 1981; 43:357-372.

[4] Van Leer B., Towards the ultimate conservative difference scheme. V, *A second order* sequel to Godunov's method. *Journal of Computational Physics*, 1979; **32**:101-136.

[5] Löhner R., 'Applied CFD Techniques', John Wiley & Sons Ltd., 2001.

[6] U. Walter, ETW User GuideETW/D/95001/ARevision A, January 2004.

[7] Zienkiewicz O., Taylor R., The Finite Element Method, Volume 1, 5th edition. Butterworth-Heinemann; 2000.